Morphology and indirect exchange coupling in Fe/Cr/Fe(110) trilayers

Jörg Schwabenhausen, Tobias Dürkop, and Hans-Joachim Elmers
Physikalisches Institut, Technische Universität Clausthal, D 38678 Clausthal-Zellerfeld, Germany
(Received 11 November 1996; revised manuscript received 18 February 1997)

We investigated the indirect exchange coupling in W(110)/Fe/Cr/Fe/Cr films. Magnetic interface anisotropies of the W/Fe and Fe/Cr interface differ in sign and thus allow the preparation of Fe films with orthogonal adjustable uniaxial anisotropies. The bilinear (J_1)and biquadratic (J_2) exchange coupling constants were determined from magnetization curves independent of magnitude and sign. We determined J_1 and J_2 as a function of Cr interlayer thickness ($t_{Cr}=0-4$ nm) and temperature ($T=100-300$ K). Moreover, we varied the morphology of the interlayer as determined by high-resolution low-energy electron diffraction using different substrate temperatures ($T_{p,Cr}=100-500$ K) during evaporation of the Cr spacer. Results for the exchange coupling versus spacer thickness are related to the particular lateral thickness fluctuation of the spacer. Our results are in good agreement with the bilinear coupling predicted by *ab initio* theories. Extrinsic biquadratic coupling models explain J_2 observed experimentally. [S0163-1829(97)03922-2]

I. INTRODUCTION

Magnetic exchange interactions between ferromagnetic films separated by nonmagnetic spacer layers[1] have been investigated to a large extent because of both possible applications exploiting the giant magnetoresistance effect[2] and the expectation of a new fundamental understanding of the nature of magnetism.[3] The exchange interaction is usually dominated by a qualitatively well-understood[4–6] Heisenberg-type interaction bilinear in the films magnetizations and oscillating in sign with increasing spacer thickness. An additional biquadratic term supporting a 90° alignment of the magnetization vectors was observed initially in Fe(100)/Cr/Fe (Ref. 7) and in Co(100)/Cu/Co.[8] Since then it has been detected in several systems (for a review see Ref. 9) and recently has attracted great attention[10–12] because the origin of the biquadratic coupling term is still an open question. Several models for its explanation considering intrinsic[13–16] and extrinsic mechanisms[17–20] have been proposed. Intrinsic models usually predict biquadratic coefficients which are 2 orders of magnitude smaller than bilinear coefficients and thus cannot explain the large experimentally values. Extrinsic models take into account the nonideal structure of the spacer layer, spatially varying thickness of the spacer,[17] loose spins in the spacer material,[19] and even pinholes through the spacer layer.[20]

In many cases the interfaces in the layered structures deviate far from the ideal interfaces. It has been shown that both bilinear and biquadratic coupling strongly depend on the interface structure[21] and alloying.[23] Obviously, a conclusive experimental study of the coupling must include a determination of the spacer structure.

One of the most frequently tested systems is the Fe/Cr system. Similar lattice constants $a_{Fe}=0.2866$ nm and $a_{Cr}=0.2886$ nm and surface energies $\gamma_{Fe}=2.9\ \mathrm{J\,m^{-2}}$ and $\gamma_{Cr}=2.0\ \mathrm{J\,m^{-2}}$ promise a layer by layer growth of Cr on Fe close to systems which can be handled by theory. This simple growth mode was indeed observed for Cr films on perfect Fe(100) whisker surfaces[22] although recent investigations[23–26] show that at the open (100) Fe/Cr interface an interface diffusion involving two monolayers (ML's) may occur even at room-temperature deposition. The layer by layer growth mode leads to the observation of a short oscillation period (2 ML) of the bilinear coupling term[27,23] in addition to the long oscillation period (9 ML) which still can be observed for a worse growth. The same long oscillation period was also found for Fe/Cr (211) (Ref. 28) and Fe/Cr(110) superlattices[29] in agreement with the theoretically predicted period.[30,5] Biquadratic coupling constants as reported for Fe/Cr(100) trilayers or superlattices by several authors[23,10,11,7] considerably vary in strength. This can be understood from the fact that the structure of the spacer plays a major role or from the fact that for the (100) symmetry a separation of the biquadratic from the bilinear term requires a careful analysis of magnetization data.[23]

We present coupling data on the Fe(110)/Cr/Fe trilayer with uniaxial anisotropies in the magnetic Fe(110) films aligned orthogonally. Recently, it was shown that in a trilayer with orthogonal uniaxial anisotropies bilinear and biquadratic coefficients can be determined in a straightforward manner independently from each other from magnetization curves.[12] In the present study we intentionally change the morphology of the Cr(110) spacer layer by varying the substrate temperature during Cr deposition on the first flat Fe(110) surface. The thickness distribution of the spacer layer was determined by high-resolution low-energy electron diffraction (HRLEED). We measured the exchange coupling for different thickness distributions and as a function of temperature in order to assess the role of loose spins and pinholes in our samples. For spacers deposited below room temperature the growth mode switches to a one-dimensional step structure thus allowing a quantitative test of extrinsic theories of the biquadratic coupling.

II. EXPERIMENT

The samples examined in this paper were deposited onto a W(110) surface by molecular-beam epitaxy. The base pressure during deposition of the films was below 1×10^{-10} mbar. Thicknesses of the films were determined by a 10

MHz quartz monitor, which was calibrated by Auger electron spectroscopy (AES). The absolute error of the layer thicknesses given below is approximately 5%. The first Fe layer with fixed thickness of 18 atomic layers was deposited onto W(110) in an optimized mode described previously,[31] starting at a substrate temperature $T_s=300$ K in order to avoid Stranski-Krastanov islanding, and raising the temperature to 600 K with increasing thickness. This procedure leads to a smooth surface with an average terrace width of 50 nm.[32] The wedge-shaped Cr spacer layer was grown at various substrate temperatures $T_{p,\mathrm{Cr}}=100-570$ K. Then, the second Fe layer of equal thickness as the first Fe layer was grown at $T_s=300$ K, avoiding any interdiffusion. At Fe(110)/Cr interfaces no interdiffusion occurs at room temperature,[33] in contrast to the observations for (100) interfaces.[23–26]

The second Fe layer was covered by additional 5 ML Cr for reasons of increased anisotropy. The coverage also serves as a protection against residual gas adsorption. All Fe and Cr layers grow pseudomorphically onto the first Fe layer preserving the (110) orientation, as was shown by LEED.

Magnetization loops were measured *in situ* using the longitudinal magneto optical Kerr effect with the external field in the plane of incidence. The angle of incidence was 15°. It was shown in Ref. 12 that the Kerr signal for this type of samples is proportional to $m(H)=m_1(H)+m_2(H)$, m_i being the magnetic moment component parallel to the external field H. This is certainly a special property of our samples and geometry.

The growth mode of the Cr interlayer as depending on the substrate temperature was determined by HRLEED in a second apparatus. The W(110)/Fe(110) base layer and the Cr layers were grown under similar conditions except that the lowest available substrate temperature for the HRLEED investigations was 230 K.

III. Cr INTERLAYER GROWTH

For characterizing the growth of the Cr interlayer, we measured LEED spot profiles of the specular beam with nearly normal incidence ($\theta=3.75°$) of the primary electrons. Parameters of the profiles were the temperature of the substrate during deposition of the Cr spacer layer $T_{p,\mathrm{Cr}}$, the average thickness D_{Cr} (in units of monolayers), $D_{\mathrm{Cr}}=t_{\mathrm{Cr}}/d_z$, with thickness t_{Cr} and layer distance $d_z=a_{\mathrm{Cr}}/\sqrt{2}$, and the incident energy E of electrons, which in our case is equivalent to the normal component $K_z=2(\sqrt{2mE}/\hbar)\cos\theta$ of the scattering vector. For fixed parameters, the reflected intensity was measured as a function of in-plane components of the scattering vector. In the following we use a Cartesian system with the x and y axes along the [001] and [110] directions. We present the reflected intensity as a function of K_x and K_y in units of $K_{1\bar{1}0}=K_{1\bar{1}}=\sqrt{2}\times 2\pi/a_{\mathrm{Cr}}=31\ \mathrm{nm}^{-1}$.

Contourlines of equidistant intensity values are shown in Fig. 1 for 3 ML Cr deposited on a smooth W(110)/Fe(110) substrate at $T_{p,\mathrm{Cr}}=230$, 350, and 450 K. The incident energy $E=120$ eV was adjusted close to an out-of-phase value, $K_z d_z/2\pi=3.5$ ($E=111$ eV), where wavelets from neighboring atomic levels are out of phase. This diffraction condition is well suited for a determination of the lateral step structure.

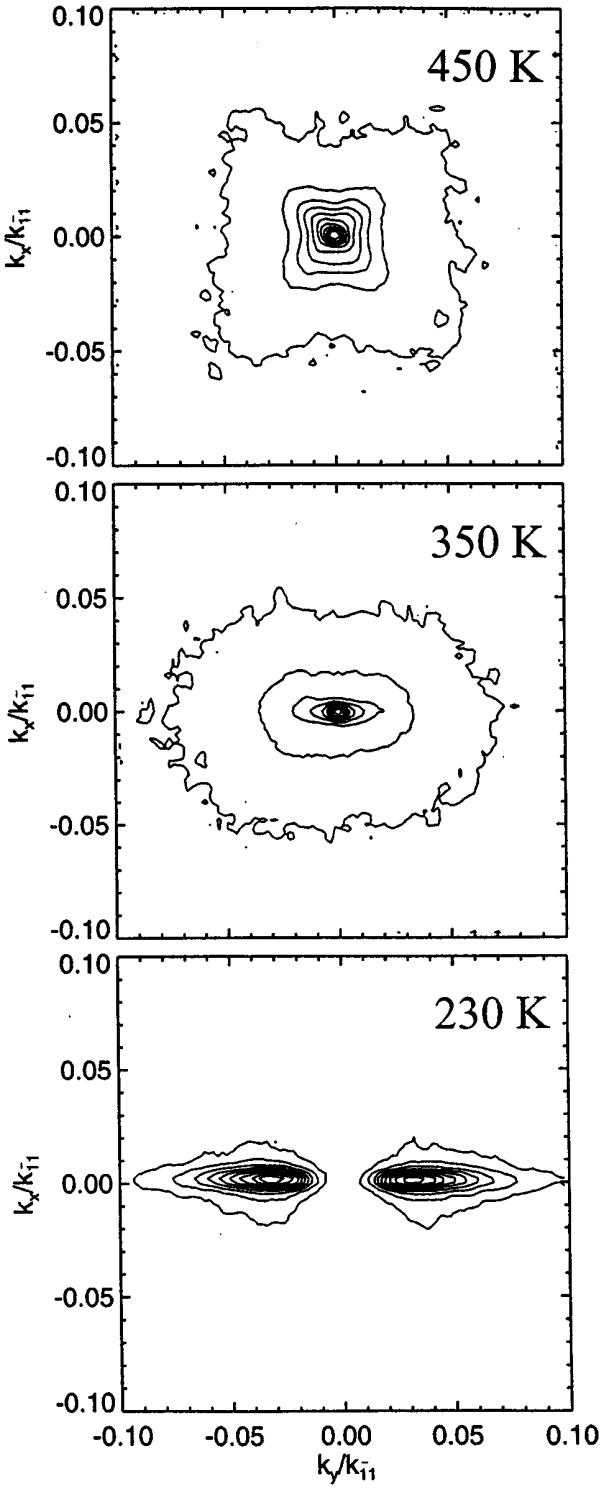

FIG. 1. Contour lines of equal intensities in the specular LEED spot for samples W(110)/18Fe/3Cr with the Cr film deposited at sample temperatures $T_{p,\mathrm{Cr}}=230$, 350, and 450 K as indicated in the figure. Kinetic energy of the electron beam near normal incidence is $E=120$ eV. Parallel components K_x and K_y of the scattering vector are normalized to $K_{1\bar{1}}=K_{1\bar{1}0}$.

For preparation at $T_{p,\mathrm{Cr}}=230$ K we observe a splitting of the specular beam in two shoulders, spread along the [110] direction. This splitting indicates a one-dimensional step structure in real space with step edges along the [001] direction.

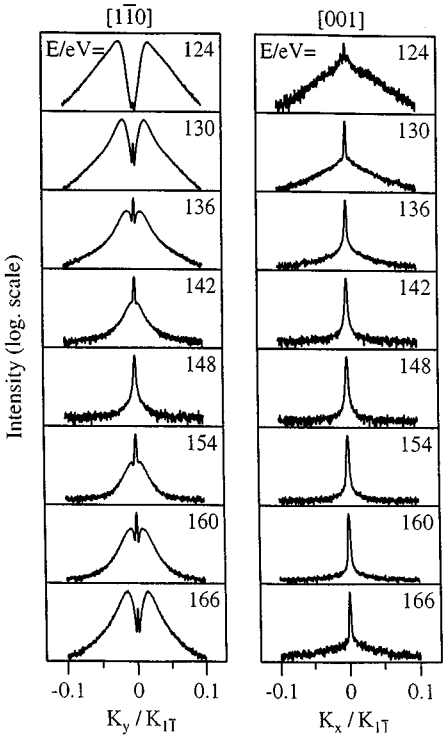

FIG. 2. Spot profiles of the specular beam along the direction of $K_{[1\bar{1}0]}$ (left panel) and $K_{[001]}$ (right panel) at incident kinetic energies E as indicated in the figure, for the sample W(110)/18Fe/3Cr with the Cr film deposited at $T_{p,\mathrm{Cr}}=230$ K. Parallel components K_x and K_y of the scattering vector are normalized to $K_{1\bar{1}}=K_{1\bar{1}0}$.

For higher deposition temperatures $T_{p,\mathrm{Cr}}=350$ and 450 K the reflected intensity switches to a two-dimensional distribution, indicating a two-dimensional step structure with step edges along several directions. A characteristic change of the intensity distribution occurs between 350 and 450 K. For 350 K deposition the contour lines are formed hexagonally whereas for 450 K deposition they show a nearly fourfold symmetry. From the width of the intensity profile at half maximum we roughly estimated mean values for the terrace widths $N(T_{p,\mathrm{Cr}})$ (in units of $d_y=0.204$ nm) and found increasing terrace widths with increasing deposition temperatures, $N(230\ \mathrm{K})=9$, $N(300\ \mathrm{K})=10$, $N(350\ \mathrm{K})=30$, $N(400\ \mathrm{K})=60$, $N(450\ \mathrm{K})=60$, and $N(500\ \mathrm{K})=100$, respectively. We also determined the terrace width for fixed $T_{p,\mathrm{Cr}}$ as a function of the Cr thickness D_{Cr} and found decreasing values for N with increasing D_{Cr}.

For the case of $T_{p,\mathrm{Cr}}=230$ K we will discuss the one-dimensional distribution of terrace widths in detail. Intensity profiles $I(E)$ along the directions of K_{10} and $K_{1\bar{1}}$ are shown in Fig. 2. Along the [110] direction we observe a pair of symmetric shoulders, which can be separated from the central spike. As K_z approaches an out-of-phase energy (111 or 182 eV) where the wavelets of neighboring levels are in antiphase, the shoulders take all of the reflected intensity and the distance of their maxima from the central peak increases with increasing deviation from the in-phase energy. Along the [001] direction the profiles only show the central peak superimposed by a homogeneous background independent of K_x. This feature again confirms that nearly all steps are along the [001] direction. The profiles for this sample are

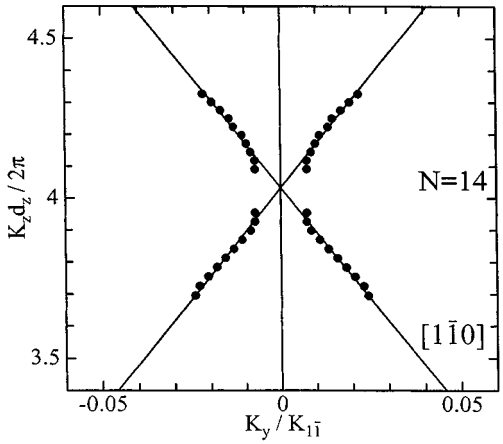

FIG. 3. Positions K_y of the shoulders in the specular spot profiles (see Fig. 2), measured along the direction of $K_{1\bar{1}}$ vs the normal component K_z of the scattering vector, for the sample W(110)/18Fe/3Cr with the Cr film deposited at $T_{p,\mathrm{Cr}}=230$ K. The mean number N of atomic rows in the steps resulting from the maximum separation in the out-of-phase scattering condition is $N=14$.

similar to those observed for homoepitaxial Fe(110) layers on Fe(110) (see Ref. 32) and we will follow the guidelines given in this reference to extract quantitative information on the structure in real space.

The positions $K_{y,0}$ of the shoulders are shown in Fig. 3 as a function of K_z. The distance between the shoulders is proportional to the deviation of K_z from the in-phase value, except for K_z very close to the in-phase scattering vector, where $K_{y,0}$ shows a finite value $K_{y,0}=0.007K_{1\bar{1}}$ independent of K_z. This behavior implicates the facet structure shown in Fig. 4. The period G of the ridge structure causes the K_z-independent shoulders appearing close to the in-phase condition[34] and can be estimated from the position $G=(0.007)^{-1}=143$ ($Gd_y=29$ nm). As was shown in Ref. 32 the maximum separation between the shoulders at an out-of-phase condition, ΔK_y is related to the number N of atomic rows per terrace, $N=K_{1\bar{1}}/\Delta K_y$ for the regular step array shown in Fig. 4. For $T_{p,\mathrm{Cr}}=230$ K we result in $N=14$. Considering a statistical distribution of terrace widths, N denotes the maximum of the distribution function, N the mean value of terrace widths.

The roughness $w=\sqrt{\langle[h(\mathbf{r})-\bar{h}]^2\rangle}$, given by the mean quadratic deviation of the height $h(\mathbf{r})$ at site $\mathbf{r}$ from the mean

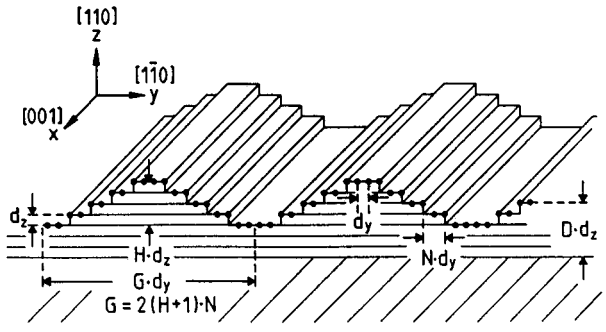

FIG. 4. Periodic triangular staircase model.

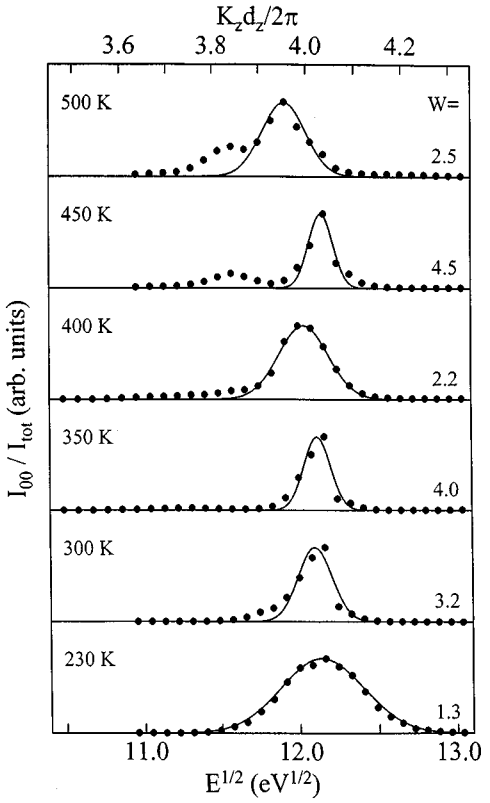

FIG. 5. Intensity I_{00} of the central spike normalized to the totally reflected intensity $I_{\rm tot}$. $I_{\rm tot}$ by integration over the $K_\parallel$ interval $|K_x|$, $|K_y|<0.1K_{1\bar{1}}$, for samples W(110)/18Fe/3Cr with the Cr film deposited at $T_{p,\rm Cr}$=230, 300, 350, 400, 450, 500 K as indicated in the figure. Full lines are fits of type $I_{00}/T_{\rm tot}\propto\exp\{-[(K_z-K_{z,n})Wd_z]^2\}$, resulting in roughness W as indicated in the figure.

height $\bar{h}$, can be determined from the intensity profile near the in-phase scattering condition, $K_{z,i}=2\pi i/d_z$. For $K_z\approx K_{z,i}$ the intensity of the central spike $I_{00}(K_z)$ normalized to the total reflected intensity $I_{\rm tot}=\int I(K_z)d\mathbf{K}_\parallel$ can be approximated by the relation[35]

$$I_{00}/I_{\rm tot}=\exp[-(K_z-K_{z,i})^2w^2]. \tag{3.1}$$

We determined $I_{00}/I_{\rm tot}$for the samples W(110)/18 Fe/3 Cr for varying deposition temperatures of the Cr film as shown in Fig. 5. For I_{00} we inserted the intensity $I(0)$ measured for $\mathbf{K}_\parallel=0$. $I_{\rm tot}$was determined from the integration of I over the $\mathbf{K}_\parallel$ interval $|K_x|,|K_y|<0.1K_{1\bar{1}}$. The roughness $W=w/d_z$ results from the fit of Eq. (3.1) to the experimental data and is indicated in the figure. We observed a strong increase of W for $T_{p,\rm Cr}$ increasing from 230 to 300 K. This is very surprising because the usual behavior is just the other way around, a smoother surface with increasing temperature. A related phenomenon might be the reentrant layer-by-layer growth observed for Pt on Pt(111) at low temperatures.[36,37] A second temperature region for a smoother surface, although pronounced more weakly, is near $T_{p,\rm Cr}$=400 K. Above this temperature $I_{00}/I_{\rm tot}$ cannot be explained by a model with single steps. A new maximum occurs for $K_zd_z/2\pi=3.8$ indicating a severe structural change. This observation coincides with a decrease of the Cr Auger signal. Presumably an interdiffusion of Cr and Fe starts at this temperature.

In the following we again discuss the results for $T_{p,\rm Cr}$=230 K in detail, where the intensity profiles can be explained completely by the facet model. Using a model with statistically distributed angles of the facets kinematic scattering theory results in[32]

$$\frac{I_{00}}{I_{\rm tot}}=\frac{1}{(H+1)^2}\,\frac{\sin^2[K_zd_z(H+1)/2]}{\sin^2(K_zd_z/2)}, \tag{3.2}$$

with H denoting the height of the facet structure as indicated in Fig. 4. The numerical result for Hobtained by a fit of this equation to the experimental data shown in Fig. 5 for $T_{p,\rm Cr}$=230 K is $H=3.3$. Of course the roughness W is related to H. Assuming the facet structure of Fig. 4 the exact relation[38] is $W^2=H^2/12+H/6$, resulting in $W=1.2$ in very good agreement with the independently determined value $W=1.3$.

Combining the information of terrace width and height of the periodic structure we determine the period G (see Fig. 4) of the ridge structure, $G=2(H+1)N$. For $T_{p,\rm Cr}$=230 K we result in $G=120$, again in agreement with the magnitude $G=143$ as determined from the spot profile $I(K_{1\bar{1}})$. For increasing thickness $D_{\rm Cr}$ we observe an increasing height of the ridge structure. Because the terrace width decreased with increasing thickness, the period G shows to be nearly independent of $D_{\rm Cr}$. The formation of the periodic step structure can be understood following the model of kinetic roughening. A barrier prevents atoms to jump between different levels, however the atoms diffuse freely on a particular atomic level until they stick at a step edge. In this layer-restricted diffusion model the period G is given approximately[32] by $G'=2N\sqrt{2\pi D}$, D representing the mean number of atomic layers. $G'=122$ (for $D_{\rm Cr}$=3) is in agreement with the experimentally determined G thus providing a strong support for this growth mode, which was also observed for Fe on Fe(110).

For $T_{p,\rm Cr}$=300 K this analysis of the intensity profiles results in a period $G=300$. At higher deposition temperatures the analysis based on a periodic model is certainly no longer appropriate. The increase both of the terrace width and the roughness with increasing $T_{p,\rm Cr}$ might indicate a monotonously increasing period G with increasing $T_{p,\rm Cr}$.

IV. MAGNETIC DATA ANALYSIS

For the data analysis we assume a homogeneous in-plane magnetization in each of both layers pointing at angles ϕ_i with respect to the external field, which was applied along the [001] axis of our samples (see Fig. 6). The idea of our method is that in Fe layer 1, in the following named the driver layer, the magnetization is fixed along the [001] direction by a very strong uniaxial anisotropy. In Fe layer 2, named sensor layer, the easy axis of the magnetization is oriented at 90° along the [110] direction. However, the uniaxial anisotropy of the sensor is weak. Then the direction of the magnetization in the sensor layer rotates from its equilibrium position under the combined action of the indirect coupling and of the external field H. Knowing the value of the weak anisotropy, the sensor magnetization thus probes the indirect coupling energy.

In order to formulate the idea quantitatively we write

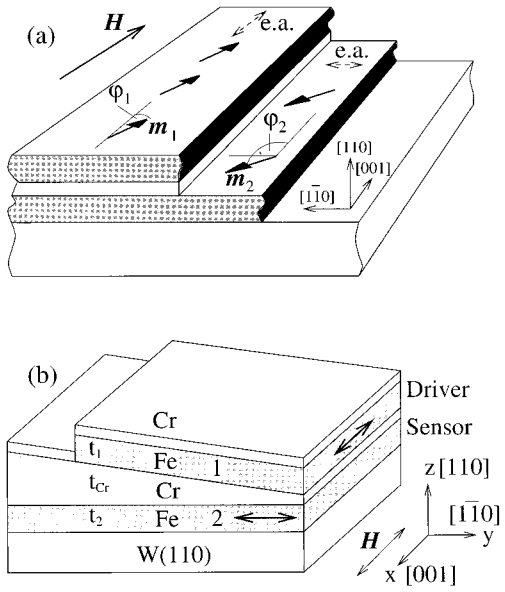

FIG. 6. (a) Schematic cross section of samples W(110)/ D_2Fe/ D_{Cr}Cr/D_1Fe/5Cr. Fe layers of thickness $t_i = D_i d_z$, number of layers D_i with distance $d_z = 0.203$ nm, are separated by a Cr spacer of thickness $t_{\mathrm{Cr}} = D_{\mathrm{Cr}} d_z$. Easy axis (e.a.) of each Fe layer is indicated in the figure. Directions of magnetic moments m_i are defined by angles ϕ_i, assuming homogeneous magnetization in each magnetic layer. (b) Schematic cross section of a typical wedge sample of linearly varying spacer thickness.

down the free enthalpy per area $g(\phi_1, \phi_2)$ of the coupled system:

$$g = (\phi_1, \phi_2) = -J_1 \cos(\phi_1 - \phi_2) - J_2 \cos^2(\phi_1 - \phi_2) - J_s t H(\cos\phi_1 + \cos\phi_2) + f_{k,1}(\phi_1) + f_{k,2}(\phi_2). \quad (4.1)$$

The indirect exchange coupling between the two magnetic Fe layers is represented by a bilinear and biquadratic coupling term with constants J_1 and J_2.The third term is the Zeeman energy per area of the magnetization in an external field H (equal film thickness t) of both Fe layers. Using the notation of Ref. 39, the anisotropy energy per area for layer (i) is given by

$$f_{k,i} = t K_p^{(i)} \cos^2\phi_i + t K_{4xy}^{(i)} \sin^2\phi_i \cos^2\phi_i, \quad (4.2)$$

$K_p^{(i)}$ and $K_{4xy}^{(i)}$ denoting the second- and fourth-order in-plane anisotropy constants. The anisotropy is a sum of volume type (index v) and surface type (index s) contributions:

$$K_p^{(i)} = K_{v,p}^{(i)} + (1/t) K_{s,p}^{(i)}, \quad (4.3)$$

$$K_{4xy}^{(i)} = K_{v,4xy}^{(i)} + (1/t) K_{s,4xy}^{(i)}. \quad (4.4)$$

For the driver layer we take the surface anisotropy constants for Cr/Fe/Cr films as determined previously,[39] see Table I. Volume anisotropy constants for the driver layer were assumed to be the same as for the sensor layer, because the pseudomorphic growth of the whole trilayer implicates the same residual strain in driver and sensor layer and hence the same magnetoelastic contribution to the volume type anisotropies. The anisotropy of the sensor layer W/Fe/Cr ($i = 2$) is crucial for the determination of coupling constants. Therefore we repeated the study of Ref. 39, resulting in slightly deviating values. Moreover, we determined $K_p^{(2)}$and $K_{4xy}^{(2)}$ explicitly for every sample and at every temperature of measurement. For this purpose a part of every sample was not covered with the driver layer.

TABLE I. In-plane anisotropy constants for driver and sensor layer as explained in the text. Effective second-order anisotropy constants $K_p'^{(i)}$ are $K_p'^{(1)} = K_p^{(1)} - K_{4xy}^{(1)}$ for the driver layer ($\phi_1 \approx 0$) and $K_p'^{(2)} = K_p^{(2)} + K_{4xy}^{(2)}$ for the sensor layer ($\phi_2 \approx \pi/2$). The thickness of the layers is $t = 3.6$ nm.

Constant	Unit	Driver ($i=1$)	Sensor ($i=2$)
$K_{s,p}^{(i)}$	mJ/m^2	$-0.42(4)$[a]	$+0.54(3)$[b]
$K_{s,4xy}^{(i)}$	mJ/m^2	$-0.14(5)$[a]	$-0.02(2)$[b]
$K_{v,p}^{(i)}$	10^5 J/m^3	$-0.78(10)$[b]	$-0.78(10)$[b]
$K_{v,4xy}^{(i)}$	10^5 J/m^3	$+0.32(5)$[b]	$+0.32(5)$[b]
$tK_p^{(i)}$	mJ/m^2	-0.70	$+0.26$
$kK_{4xy}^{(i)}$	mJ/m^2	-0.02	$+0.09$
$tK_p'^{(i)}$	mJ/m^2	-0.68	$+0.35$

[a]From Ref. 39.
[b]This work.

As long as $K_p^{(i)}/K_{4xy}^{(i)} > 1$, the direction of the easy axis is either [001] or [110] and determined by the sign of the second-order constant, $K_p^{(i)}$. For the driver layer the volume type and both interface anisotropies have the same sign and add up to the desired strong easy axis along [001], $K_p^{(i)} < 0$. For the sensor layer the strong interface anisotropy of the W/Fe interface supports an easy axis along [110] whereas the volume type anisotropy has an easy axis along [001]. By varying the thickness of the sensor layer we can thus control the anisotropy in the sensor layer in a wide range. For the thickness $t = 3.6$ nm of both Fe layers, which was fixed in this study, values are summarized in Table I.

Qualitative insight is obtained by the following rigid driver approximation. A weak-coupling energy $|J_1|, |J_2| < |K_p^{(1)}|$ with respect to the driver layer anisotropy leaves the magnetization of the driver layer nearly locked (for decreasing field values) along the direction of the external field, i.e., $\phi_1 = 0$. For a small deviation of ϕ_2 from equilibrium position $\phi_2 \approx \pi/2$ we can describe the sensor anisotropy by an effective anisotropy term $K_p' \cos^2\phi_2$ of second order only with $K_p' = K_p + K_{4xy}$. Equation (4.2) then simplifies to the rigid driver approximation:

$$g(\phi_2) = (tK_p' - J_2)\cos^2\phi_2 - (J_1 + J_s t H)\cos\phi_2. \quad (4.5)$$

Minimization of g results in $\cos\phi_2 = (J_1 + J_s t H)/2(tK_p' - J_2)$. From $\cos\phi_2(H_A) = 0$ we determine the bilinear constant, $J_1 = -J_s t H_A$ and from the initial increase of $\cos\phi_2(H)$ the biquadratic constant J_2. Hence, $J_1$and J_2 can be determined from the sensor magnetization curve independently from each other. Certainly, the rigid driver model is valid only for the approximation of weak-coupling constants. In general, magnetization curves generated by minimization of the exact free enthalpy [Eq. (4.2)] are fitted to the experimental curves with J_1 and J_2 as parameters. As long as J_1 and J_2 are small with respect to the anisotropy constant K_p' both parameters

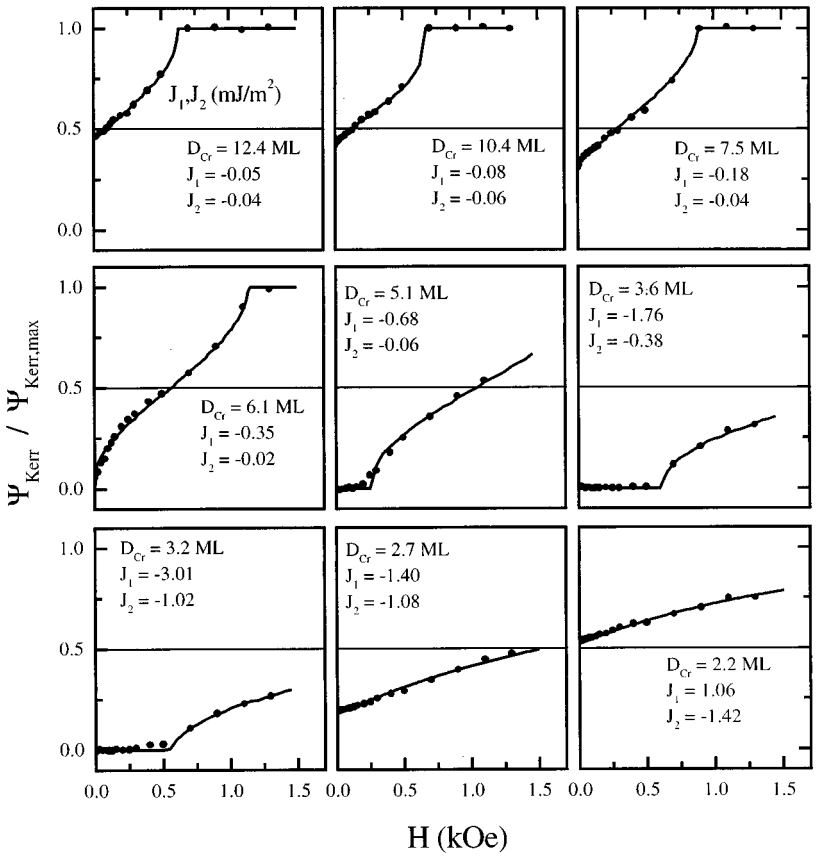

FIG. 7. Magnetization loops represented by normalized Kerr rotations $\Psi_{\mathrm{Kerr}}/\Psi_{\mathrm{Kerr,max}} = m/m_{\mathrm{sat}}$ vs external field H for samples W(110)/18Fe/D_{Cr}Cr/18Fe/5Cr, consisting of 2 Fe layers of 18 atomic layers each, separated by a Cr spacer consisting of D_{Cr} atomic layers, and covered by a cap layer of 5 atomic layers of Cr. $D = 18$ of the Fe layers and spacer thickness D_{Cr} as included in the figure. Data are measured for decreasing field, only (full circles). Full lines are fitting curves from minimization of g, resulting in the coupling parameters J_1, J_2 (in mJ/m^2) as indicated in the figure.

result independently from each other from the fit. For large interlayer coupling, J_1 and J_2 are related to some extent, thus resulting in an increasing error as discussed below.

V. RESULTS

Figure 7 shows experimental magnetization curves from a sample with wedgelike varying spacer thickness D_{Cr}. We measure the Kerr rotation Ψ_{Kerr}, normalized to the saturation value, $\Psi_{\mathrm{Kerr,max}}$, which was assumed to be proportional to the magnetization component parallel to the external field. Simulated magnetization curves using the free enthalpy model given by Eq. (4.2) were fitted to the experimental data with parameters J_1 and J_2. For the fit we only use magnetization data measured at decreasing absolute field values, in order to avoid metastable magnetization states. When the interlayer coupling is weak, as in the case of $D_{\mathrm{Cr}}=12.4$ ML, we observe a magnetization curve composed of the sum of the constant easy axis signal of the driver layer and the hard axis curve of the sensor layer. At $H=0$ we only see the signal of the driver layer. The sensor layer signal increases with H, the nonlinear jump to the saturation state at $H=0.6$ kOe is caused by the fourth-order anisotropy term. In the saturated state the signal is twice as large as the remanent signal, thus confirming that magnetization components of sensor and driver layer contribute equally to the total signal. For decreasing D_{Cr} the sensor curve is shifted to positive fields indicating an increasing antiferromagnetic coupling $J_1<0$. For $D_{\mathrm{Cr}}<5$ ML the slope of the sensor curve at $\Psi_{\mathrm{Kerr}}/\Psi_{\mathrm{Kerr,max}}=0.5$ is decreased and prevents the signal from saturation. This observation indicates a strong 90° coupling, $J_2<0$.

For the strongest indirect coupling and small field, the magnetization directions are aligned antiparallel to each other. The critical field H_c needed to get the onset of noncollinear configuration can be estimated by the following consideration. At H_c both magnetization directions start to deviate from $\phi_1=0$ and $\phi_2=\pi$. We assume small deviations angles $xi, \delta \ll 1$, i.e., $\phi_1=\sqrt{2}\xi$ and $\phi_2=\pi+\sqrt{2}\delta$. At some critical field the gain of free enthalpy $\Delta g = g(0,\pi) - g(\sqrt{2}\xi, \pi+\sqrt{2}\delta)$ becomes positive and the magnetization directions will deviate from the antiparallel alignment. In a quadratic approximation this condition results in the critical field H_c

$$H_c = H_A \frac{(\xi-\delta)^2}{\delta^2-\xi^2} + H_{k,1}\frac{\xi^2}{\delta^2-\xi^2} + H_{k,2}\frac{\delta^2}{\delta^2-\xi^2}, \quad (5.1)$$

with the effective fields $H_A=(-J_1+2J_2)/J_s t$ and $H_{k,i}=-2(K_p^{(i)}-K_{4xy}^{(i)})/J_s$. The effective anisotropy field of the driver layer is $H_{k,1}=1.1$ kOe and of the sensor layer $H_{k,2}=-0.3$ kOe. Therefore the deviation of the driver magnetization ξ is smaller than the deviation of the sensor layer δ. In a rough approximation the ratio is given by $\delta = |H_{k,1}/H_{k,2}|\xi = 3.5\xi$. With these values we result in $H \geqslant 0.6$ kOe both for the bottom left case ($D_{\mathrm{Cr}}=3.2$ ML) and for the right center row ($D_{\mathrm{Cr}}=3.6$ ML) of Fig. 7 in good agreement with the exact calculation.

Results for the bilinear coupling J_1 as a function of interlayer thickness are summarized in Fig. 8(a). For the case of weak-coupling constants $J_1, J_2 < 0.1$ mJ/m^2 we avoided the elaborate fit procedure and present the data resulting from the rigid driver model instead. At some points we checked

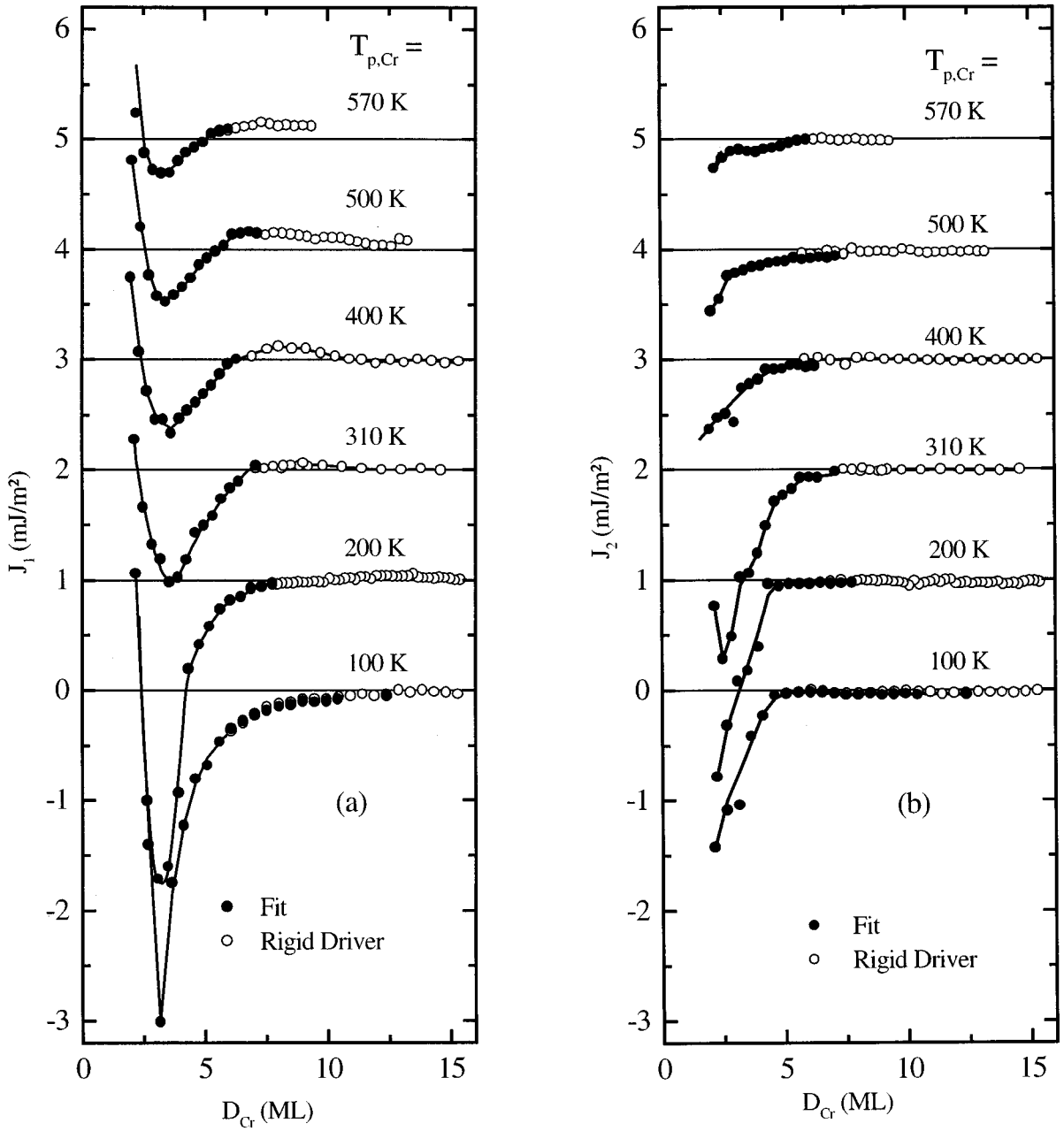

FIG. 8. Coupling parameters J_1 (a) and J_2(b) vs D_{Cr} for samples W(110)/ DFe/D_{Cr}Cr/DFe/5Cr. The parameter $T_{p,\mathrm{Cr}}$ indicates the sample temperature during deposition of the Cr spacer layer. Full circles result from numerical fits of simulated magnetization curves resulting from minimization of g, open circles from rigid driver approximations. Full lines are guide-to-the-eye curves.

that for such small coupling constants values resulting from both evaluation procedures are equal. Independent of $T_{p,\mathrm{Cr}}$, J_1 shows a sharp transition from a ferromagnetic coupling for $D_{\mathrm{Cr}}<D_0=(2.5\pm0.1)$ ML to an antiferromagnetic coupling at $D_{\mathrm{Cr}}>D_0$, followed by a minimum value at $D_{\mathrm{Cr}}=D_1=(3.4\pm0.1)$ ML. For the lowest deposition temperature, $T_{p,\mathrm{Cr}}=100$ K, J_1 remains negative up to the thickest Cr thickness used in this study, $D_{\mathrm{Cr}}=15$ ML. In this case no indication of an oscillation of J_1 was observed. For higher deposition temperatures J_1 changes its sign a second time at $D_{\mathrm{Cr}}=D_2\approx7$ ML. D_2 decreases with increasing deposition temperature.

The biquadratic coupling J_2 shown in Fig. 8(b) shows negative values (90° coupling) at $D_{\mathrm{Cr}}=2.5$ ML decreasing towards $J_2=0$ at $D_{\mathrm{Cr}}=5-7$ ML. For $D_{\mathrm{Cr}}<2.5$ ML the error both for J_1 and J_2 increases considerably due to the strong coupling between the two parameters. Therefore coupling data are not available for $D_{\mathrm{Cr}}<D_0$. The largest 90° coupling magnitudes were observed for the interlayer deposited at room temperature (see Ref. 12). We did not find positive values for J_2 although our model would have been able to detect them.

The antiferromagnetic extremum $J_1(D_1)$ of the bilinear coupling constant is shown in Fig. 9 as a function of the interlayer deposition temperature. We found a surprising large antiferromagnetic coupling for $T_{p,\mathrm{Cr}}$ below room temperature. $|J_1(D_1)|$ increased by a factor of 3 when $T_{p,\mathrm{Cr}}$ is decreased below room temperature. Deposition above room

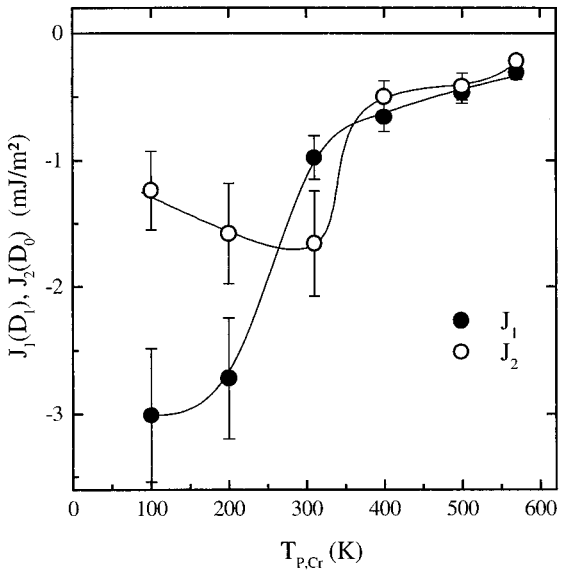

FIG. 9. Maximum antiferromagnetic coupling constant $J_1(D_1)$ observed at a spacer thickness $D_1=3.4$ ML and biquadratic coupling constant $J_2(D_0)$ at spacer thickness $D_0=2.5$ ML where the bilinear coupling changes sign vs deposition temperature $T_{p,\mathrm{Cr}}$. Full lines are guide-to-the-eye curves.

temperature results in gradually decreasing values of $|J_1(D_1)|$ with increasing $T_{p,\mathrm{Cr}}$. We show data for the biquadratic coupling constant $J_2(D_0)$ observed for an interlayer thickness $D_0=2.5$ ML where J_1 changes its sign for the first time. J_2 could still be determined with satisfying accuracy for this interlayer thickness. The 90° coupling $|J_2|$ slightly increases with increasing $T_{p,\mathrm{Cr}}$ from 100 to 310 K. This increase is not significant with respect to the error bars. For further increased $T_{p,\mathrm{Cr}}\geqslant 400$ K, however, $|J_2|$ is strongly reduced.

VI. DISCUSSION

The main purpose of this paper is the study of the influence of the morphology of the interlayer on the indirect coupling. Because the Cr interlayer was grown on a smooth Fe(110) surface, one of the interlayer interfaces is flat. The structure of the second interface is known from the HRLEED investigation. Consequently, we know the lateral distribution of the interlayer thickness D_{Cr}. Unfortunately, we could not reach layer by layer growth of the interlayer. Therefore, we could not determine directly the bilinear coupling constant J_1 as a function of a virtually constant interlayer thickness.

Because of the inhomogeneous interlayer thickness and the corresponding inhomogeneous interlayer coupling we have to consider inhomogeneous magnetization directions within the Fe layers. For this purpose the length scale of the lateral D_{Cr} distribution has to be compared with the magnetic exchange length $2l$ in the sensor layer. The relevant exchange length $2l=\sqrt{4A/K_p'}=29$ nm in our samples can be estimated, using the bulk value for the exchange constant $A=2\times10^{-11}$ J/m and the effective anisotropy constant $tK_p'=0.35$ mJ/m^2 of the sensor layer. For deposition temperatures $T_{p,\mathrm{Cr}}\leqslant 300$ K the terrace width $Nd_y\approx 2$ nm of the Cr interlayer is much smaller than $2l$. Even the period of the ridge structure $Gd_y=29$ nm is still of the order of magnitude of the exchange length. In this case the magnetization vector oscillates around a mean direction given by ϕ_2, with a small amplitude, thus satisfying the local bilinear coupling to some extent. As discussed by Slonczewski[17] the latter effect gives rise to an effective 90° coupling term (J_2) but the homogeneous magnetization model as declared in Eq. (4.2) is still valid. Moreover, for strong antiferromagnetic coupling $-J_1 \gg tK_p'$ and vanishing external field one expects (in the case of homogeneous magnetization) a compensation of the driver layer and sensor layer signal. This was observed in the experiment (see Fig. 7). Contrarily, in the case of strongly inhomogeneous magnetization, one would have expected a superposition of magnetization curves from independent antiferromagnetic and ferromagnetic regions. Then the ferromagnetic coupled regions showing easy axis hysteresis loops would have resulted in a considerable remanent signal. This argument again supports our model of virtually homogeneous magnetization.

There has been an attempt to explain the biquadratic coupling component by an intrinsic electronic mechanism. However, the values predicted by these models are 1–2 orders of magnitude too small to explain our experimental data. Extrinsic models that we take into account are the loose spin mechanism, pinholes through the spacer layer and Slonczewski's mechanism of interfacial roughness. The loose spin mechanism would result in a strong decrease of $|J_2|$ with increasing temperature. Because in our case J_2 does not vary with the temperature this mechanism can be excluded. Ferromagnetic pinholes in the spacer with a size larger than the exchange length would have caused a superposition of easy axis loops which was not observed. The effect of pinholes which are small enough to allow for a homogeneous magnetization can in principle not be distinguished from the effect of interfacial roughness, which shall be discussed below in detail.

Slonczewski[17] showed how spatial fluctuations of the local bilinear coupling $J_1(x)$ caused by spatial fluctuations of the spacer layer thickness account for an effective biquadratic coupling. In the simplest version of the model J_1 is a (one-dimensional) periodic step function $J_1=J_1+\Delta J_1 \mathrm{sgn}\sin(\pi x/L)$ with the period L and amplitude ΔJ_1. This assumption results in a biquadratic coupling constant

$$J_2=-\frac{4(\Delta J_1)^2 L}{\pi^3 A}\coth(\pi t/L). \tag{6.1}$$

Slonczewski considered a thickness fluctuation of only 1 atomic layer of a Cr(100) interlayer. For the Cr(100) interlayer the bilinear coupling J_1 shows opposite signs for odd and even numbers of atomic layers. These short period oscillations cannot be expected for Cr(110) layers because the magnetic moments of antiferromagnetic Cr cancel in the (110) plane. However, the one-dimensional ridge structure of the (110) spacer layer deposited at $T_{p,\mathrm{Cr}}=230$ K causes a fluctuating bilinear coupling similar to the model structure described above. When the average thickness of the spacer is thin, the roof tops of the ridge structure provide regions with antiferromagnetic coupling whereas in the valleys the coupling is ferromagnetic due to the long period oscillation of

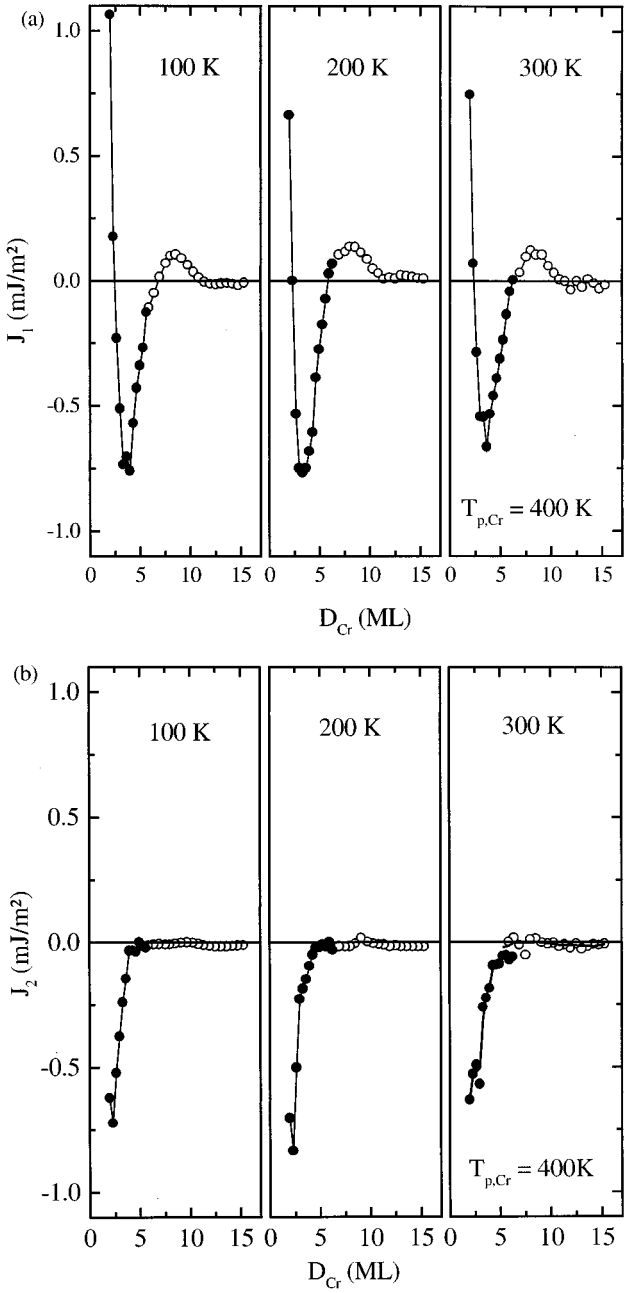

FIG. 10. Coupling parameters J_1 (a) and J_2 (b) vs D_{Cr} for samples W(110)/18Fe/ D_{Cr}Cr/18Fe/5Cr with the spacer deposited at $T_{p,\mathrm{Cr}}=400$ K, measured at temperatures $T=100$, 200, and 300 K. Symbols and full lines as in Fig. 8.

bilinear coupling. Hence, the coupling constant J_1 can be described by the same function as in Ref. 17 to a very good approximation. Now, the meaning of L in Eq. (6.1) is not the terrace width but the period of the ridge structure G. We estimate the amplitude $\Delta J_1=3$ mJ/m^2 at the spacer thickness D_0 where J_1 changes it sign from the maximum value observed for J_1. Inserting the period of the ridge structure ($L=G=29$ nm for $T_{p,\mathrm{Cr}}=230$ K and $L=G=61$ nm for $T_{p,\mathrm{Cr}}=300$ K) and the Fe layer thickness $t=3.6$ nm, Eq. (6.1) results in $J_2=-4.5$ mJ/m^2 ($T_{p,\mathrm{Cr}}=230$ K) and $J_2=-9.5$ mJ/m^2 ($T_{p,\mathrm{Cr}}=300$ K). These values are in sufficient agreement with the experimentally observed magnitude $J_2=-1.6$ mJ/m^2 to support the model. Detailed micromagnetic calculations taking into account the ridge structure of the spacer are highly desirable.

The weak increase of $|J_2(D_0)|$ with $T_{p,\mathrm{Cr}}$ increasing from $J_2=-1.2$ mJ/m^2 at 100 K to $J_2=-1.8$ mJ/m^2 at 310 K might be a result of the increasing period of the ridge structure with increasing deposition temperature. An increase of the period directly results in an increase of bilinear coupling [Eq. (6.1)]. However, the experimentally observed increase is much lower than expected from Eq. (6.1). For $T_{p,\mathrm{Cr}}=310$ K we observed a structural change of the spacer from the one-dimensional ridge structure to a two-dimensional pattern. A spatially fluctuating J_1 in two dimensions will also result in a biquadratic coupling but with a reduced magnitude. This reduction compensates the increase caused by the period to some extent. For higher deposition temperatures $T_{p,\mathrm{Cr}}\geqslant 400$ K the biquadratic coupling becomes rather weak although the period G increases monotonously. However, Eq. (6.1) is not valid when the period exceeds the exchange length. This is very likely the case for high deposition temperatures.

We now discuss the thickness dependence of J_2. From Fig. 8(b) we see that the biquadratic coupling constant J_2 shows only negative values as expected from Eq. (6.1). $|J_2|$ is largest for small Cr thicknesses. As explained above the experimental error of J_2 increases drastically for Cr thicknesses below $D_{\mathrm{Cr}}=D_0$. Therefore no unequivocal maximum of $|J_2|$ could be detected, except in the case of $T_{p,\mathrm{Cr}}=310$ K. Our model of fluctuating bilinear coupling at ridges and valleys would result in an extremum for J_2 at the spacer thickness D_0 where J_1 changes sign: An increasing spacer thickness reduces the ferromagnetic coupling in the valleys whereas the average antiferromagnetic coupling at the ridges is nearly constant or even reduced. Thus, the amplitude ΔJ_1 rapidly decreases with increasing D_{Cr}. Consequently, $|J_2|$ will decrease as observed in the experiment. A quantitative analysis of the thickness dependence requires a micromagnetic analysis.

A similar monotonously decreasing $|J_2|$ with increasing D_{Cr} was observed in the case of Fe/Cr/Fe in the (100) orientation.[11] In this reference the authors described the thickness dependence of J_2 by a power law $|J_2|\propto D_{\mathrm{Cr}}^{-1.4}$. Our results for $J_2(D_{\mathrm{Cr}})$ cannot be described with such a unique power law.

Our experimental data for the bilinear coupling J_1 can be compared with theoretical considerations. Stiles[4] recently calculated the strength and period of oscillatory exchange coupling for Fe/Cr layers by first-principle methods. For the (110) orientation he found for the strongest long period oscillation a coupling strength $t_{\mathrm{Cr}}^2 J_1/(1.0)$ nm$^2=-3.2$ mJ/m^2. For the case of the first antiferromagnetic maximum at $t_{\mathrm{Cr}}=0.7$ nm the theoretical value is $J_1=-6.5$ mJ/m^2. Previously measured coupling strengths for Fe/Cr were much smaller than the calculated values. Our measured maximum of antiferromagnetic coupling (for low temperature deposition of the Cr) is exceptionally large and reaches nearly half of the theoretical value. This is very surprising taking into account the fluctuating spacer thickness still observed for the low temperature deposition. At $D_{\mathrm{Cr}}=3$ ML$\approx D_1$ the height $H=3$ of the ridge structure is considerable. Following Ref. 17 the measured value of J_1 is the

mean value of the contributions from different interlayer thicknesses, $J_1(D_{Cr})=\Sigma_n J_1(n)p(n,D_{Cr})$, where the contribution from the coupling constant $J_1(n)$ at the interlayer thickness n is weighted with the probability $p(n,D_{Cr})$ of the occurrence of interlayer thickness n at a total deposited thickness D_{Cr}. The function $p(n,D_{Cr})$ is not known exactly in our case and it is impossible to extract $J_1(n)$ from $J_1(D_{Cr})$. However, the maximum antiferromagnetic coupling constant $J_1(D_1)$ observed in our experiment for low-temperature deposition is in good agreement with the theoretically predicted value.

The sharp decrease of $|J_1(D_1)|$ for deposition temperatures $T_{p,Cr}\geqslant 310$ K coincides with the increase of the roughness W. An increase of W will certainly result in a broader distribution $p(n,D_{Cr})$ and consequently in a decrease of maximum values. Especially, contributions from thin interlayer thicknesses $n=0$ and 1 with presumably very strong ferromagnetic coupling will rapidly decrease the antiferromagnetic coupling. This may explain the nonlinear decrease of $|J_1(D_1)|$ near $T_{p,Cr}=310$ K although the increase of the roughness is rather small.

The origin of the ferromagnetic maximum near $D_{Cr}=8$ ML appearing for $T_{p,Cr}\geqslant 310$ K apparently is an oscillating bilinear coupling $J_1(n)$, significantly damped by the fluctuating spacer thickness. The oscillation period $\Lambda\approx 2$ nm estimated from the half period observed in our experiment coincides with the long wavelength period as determined both for the (100) and for the (211) orientation.[28] This surprising independence of the long-wavelength period on the orientation has been attributed to either a lens structure near the center of the Cr Fermi surface[40] or to the N-centered ellipsoids.[4] From our results we would not distinguish between these two alternative explanations.

For higher deposition temperatures $T_{p,Cr}\geqslant 500$ K we observed a nonvanishing ferromagnetic coupling $J_1>0$ even for interlayer thicknesses $D_{Cr}>12$ ML [see Fig. 8(a)]. This effect is presumably caused by the onset of interdiffusion. It is quite plausible that Fe-rich Fe/Cr alloy regions produced by the interdiffusion enhance the ferromagnetic coupling.

As expected, we did not observe any significant temperature dependence of J_1 [see Fig. 10(a)]. From theoretical considerations the temperature dependence of J_1 should follow the temperature dependence of the magnetization J_s of the Fe layers.[5] Since the Curie temperature of the Fe layers is far above room temperature, J_s is expected to be nearly constant for the range of temperatures applied in our experiment.

VII. SUMMARY

We determined bilinear and biquadratic coupling constants in Fe/Cr/Fe(110) trilayers for varying spacer morphologies. The large coupling constants occurring for spacer layer deposition below room temperature exceed previously reported values. The bilinear coupling constant does not depend significantly on the temperature of measurement in the interval $T=100$–300 K. The maximum value of the antiferromagnetic coupling is in agreement with theoretical calculations using *ab initio* methods. The biquadratic coupling can be explained from the fluctuating bilinear coupling caused by the rough interface. We compared experimental data with Slonczewski's micromagnetic model.

ACKNOWLEDGMENTS

The authors are indebted to U. Gradmann for valuable suggestions and discussions on the results presented in this paper.

[1] P. Grünberg, R. Schreiber, Y. Pang, M. B. Brodsky, and H. Sowers, Phys. Rev. Lett. **57**, 2442 (1986).
[2] M. N. Baibich, J. M. Broto, A. Fert, F. Nguyen Van Dau, F. Petroff, P. Etienne, G. Creuzet, A. Friederich, and J. Chazelas, Phys. Rev. Lett. **61**, 2472 (1988).
[3] *Ultrathin Magnetic Structures*, edited by J. A. C. Bland and B. Heinrich (Springer, Berlin, 1994), Vol. II.
[4] M. D. Stiles, Phys. Rev. B **54**, 14 679 (1996).
[5] M. D. Stiles, Phys. Rev. B **48**, 7238 (1993).
[6] P. Bruno and C. Chappert, Phys. Rev. B **46**, 261 (1992).
[7] M. Rührig, R. Schäfer, A. Hubert, R. Mosler, J. A. Wolf, S. Demokritov, and P. Grünberg, Phys. Status Solidi A **125**, 635 (1991).
[8] B. Heinrich, J. Kirschner, M. Kowalewski, J. F. Cochran, Z. Celinski, and A. S. Arrot, Phys. Rev. B **44**, 9348 (1991).
[9] A. Fert and P. Grünberg, J. Magn. Magn. Mater. **140-144**, 1 (1995).
[10] A. Azevedo, C. Chesman, S. M. Rezende, F. M. de Aguiar, X. Bian, and S. S. P. Parkin, Phys. Rev. Lett. **76**, 4837 (1996).
[11] R. J. Hicken, C. Daboo, M. Gerster, A. J. R. Ives, S. J. Gray, and J. A. C. Bland, J. Appl. Phys. **78**, 6670 (1995).
[12] H. J. Elmers, G. Liu, H. Fritzsche, and U. Gradmann, Phys. Rev. **B52**, R696 (1995).
[13] R. P. Erickson, K. B. Hathaway, and J. R. Cullen, Phys. Rev. B **47**, 2626 (1993).
[14] D. M. Edwards, J. M. Ward, and J. Mathon, J. Magn. Magn. Mater. **126**, 380 (1993).
[15] J. D. A. Castro, M. S. Ferreira, and R. B. Muniz, Phys. Rev. B **49**, 16 062 (1994).
[16] J. Inoue, J. Magn. Magn. Mater. **136**, 233 (1994).
[17] J. C. Slonczewski, Phys. Rev. Lett. **67**, 3172 (1991).
[18] S. Demokritov, E. Tsymbal, P. Grünberg, W. Zinn, and I. K. Schuller, Phys. Rev. B **49**, 720 (1994).
[19] J. C. Slonczewski, J. Appl. Phys. **73**, 5957 (1993).
[20] J.-F. Bobo, M. Piecuch, and E. Snoek, J. Magn. Magn. Mater. **126** 440 (1993).
[21] B. Heinrich, Z. Celinski, J. F. Cochran, A. S. Arrot, K. Myrtle, and S. T. Purcell, Phys. Rev. B **47**, 5077 (1993).
[22] J. A. Stroscio, D. T. Pierce, J. Unguris, and R. J. Celotta, J. Vac. Sci. Technol. B **12**, 1789 (1994).
[23] B. Heinrich, J. F. Cochran, D. Venus, K. Totland, D. Atlan, S. Govorkov, and K. Myrtle, J. Appl. Phys. **79**, 4518 (1996).
[24] D. Venus and B. Heinrich, Phys. Rev. B **53**, R1733 (1996).
[25] A. Davies, J. A. Stroscio, D. T. Pierce, and R. J. Celotta, Phys. Rev. Lett. **76**, 4175 (1996).
[26] R. Pfandzelter, T. Igel, and H. Winter, Phys. Rev. B **54**, 4496 (1996).
[27] J. Unguris, R. J. Celotta, and D. T. Pierce, Phys. Rev. Lett. **67**, 140 (1991).

[28] E. E. Fullerton, J. E. Mattson, C. H. Sowers, and S. D. Bader, Scr. Metall. Mater. **33**, 1637 (1995).
[29] S. S. P. Parkin, Phys. Rev. Lett. **67**, 3598 (1991).
[30] M. van Schilfgaarde, F. Herman, S. S. P. Parkin, and J. Kudrnovsky, Phys. Rev. Lett. **74**, 4063 (1995).
[31] H. J. Elmers and U. Gradmann, Appl. Phys. A **51**, 255 (1990).
[32] M. Albrecht, H. Fritzsche, and U. Gradmann, Surf. Sci. **294**, 1 (1993).
[33] J. Zukrowski, G. Liu, H. Fritzsche, and U. Gradmann, J. Magn. Magn. Mater. **145**, 57 (1995).
[34] M. Horn van Hoegen (private communication).
[35] H. N. Yang, G. C. Wang, and T. M. Lu, *Diffraction from Rough Surfaces and Dynamic Growth Fronts* (World Scientific, Singapore, 1993).
[36] R. Kunkel, B. Poelsema, L. K. Verheij, and G. Comsa, Phys. Rev. Lett. **65**, 733 (1990).
[37] P. Smilauer, M. R. Wilby, and D. Vvedensky, Phys. Rev. B **47**, 4119 (1993).
[38] H. Fritzsche, Ph.D thesis, Clausthal, 1995.
[39] H. Fritzsche, H. J. Elmers, and U. Gradmann, J. Magn. Magn. Mater. **135**, 343 (1994).
[40] D. D. Koelling, Phys. Rev. B **50**, 273 (1994). For a review of Cr Fermi surfaces see E. Fawcett, Rev. Mod. Phys. **60**, 209 (1988).